Article

Analysis of Urban Expansion and Heat-Island Effect of Hefei Based on ENVI

Junlei Meng [1,*] and Yang Gao [2,3]

1   College of Oceanic and Atmospheric Sciences, Ocean University of China, Qingdao 266100, China
2   Key Laboratory of Marine Environmental Science and Ecology, Ministry of Education,
    Ocean University of China, Qingdao 266100, China; yanggao@ouc.edu.cn
3   Sanya Oceanographic Institution, Ocean University of China, Sanya 572024, China
*   Correspondence: mjl@stu.ouc.edu.cn; Tel.: +86-180-5323-3728

Abstract: Urbanization is one of the most significant features of current social progress. Using Landsat TM/OLI images from 1995, 2005, and 2018, the land-use change, vegetation coverage, and land surface temperature retrieval of Hefei are studied, and the driving force of Hefei's expansion is analyzed. The influence of urban expansion and vegetation coverage on the intensity of the urban heat-island effect is discussed. As the city develops, various factors, such as natural conditions, economic growth, demographic changes, and policy decisions, are driving the expansion of construction land in Hefei. The overall performance shows expansion to the southwest of the main urban area, the surface temperature rises as the city expands, and the area of the heat-island effect also increases, showing the trend of multi-center distribution. There is a clear negative correlation between land surface temperature and vegetation coverage. Therefore, increasing the city's green infrastructure can effectively alleviate the severe heat-island effect.

Keywords: urbanization; urban expansion; construction land; vegetation coverage; heat-island effect

1. Introduction

A city is a gathering point for human beings' unique gathering space and various activities. At this stage, it is undoubtedly the "regulatory center" for the evolution of the Earth [1]. From the perspective of demography, cities are areas where the population is highly concentrated; population size and density are the criteria for judging a city. From the perspective of geography, cities are spatial settlements that differ from rural areas in terms of industry, population, and architectural space. From the perspective of economics, cities are economic units based on a social division of labor, a center of high concentration of economic activities, and market exchanges [2]. From a sociological perspective, cities are forms of social organization with defined characteristics and geographic boundaries [3].

Urbanization is mainly manifested in the process of urban population increase, accompanied by a series of changes in social, economic, cultural, and natural landscapes, which is a complex evolutionary process [4]. With economic development, the continuous expansion of urban scale, and the rapid increase of the urban population, urbanization is rapidly transforming agricultural land into urban construction land [5]. One of the important characteristics of rapid urbanization is the accelerated spatial and temporal evolution of urban construction land [6,7]. Therefore, the expansion of urban construction land has not only become an important measure for evaluating the urbanization level but also an important area of research for land-use-/-cover change. At the same time, the expansion of urban construction land is the most direct way to influence regional temperature in the process of urbanization [8].

In recent years, intensified human activities in urban areas have had a significant impact on the ecological environment, leading to the formation of the urban heat-island effect. This phenomenon arises from changes in the local heat balance, which create

notable temperature disparities between urban centers and their suburban surroundings [9]. Recognized as a crucial indicator of the severity of urbanization [10], the urban heat-island effect has garnered increasing attention. Larger cities with denser populations typically exhibit more pronounced heat-island effects that are influenced by geographical factors, city layout, industrial activities, and human-generated heat emissions [11]. Numerous studies highlight strong correlations between the formation of the heat-island effect and weather conditions, such as wind-speed and cloud-cover variations [12,13]. Research across disciplines has explored the distribution, mechanisms, and impacts of the heat-island effect, revealing its contribution to phenomena such as urban rain islands, which concentrate heavy rainfall and cause waterlogging in megacities [14]. The heat-island effect significantly influences urban climate dynamics, with impervious urban surfaces like concrete and tiles intensifying heat retention, while vegetated areas with soil and water generally maintain cooler temperatures [15]. Consequently, there is an urgent need to intensify research on mitigating the heat-island effect, with a focus on developing comprehensive strategies to promote healthier urban environments.

Remote sensing is a kind of detection technology, and its application in various fields has become increasingly mature. Remote sensing has been widely used in agricultural production, land use, land and resources management, atmospheric monitoring, and other aspects [16]. However, when using remote-sensing technology for land-use research, many scholars in China tend to focus on large cities, often neglecting smaller developing cities [17]. Hefei, the capital of Anhui Province, is one such city. Despite being a provincial capital, Hefei has unique characteristics that distinguish it from other capitals. Its rapid urbanization, significant economic growth, and strategic location within the Yangtze River Delta Economic Zone make it an ideal case study for understanding urban expansion, land-use changes, and the urban heat-island effect [18].

We selected the time period from 1995 to 2018 for this study to capture the extensive urban development that Hefei has undergone in recent decades. This period allows us to analyze long-term trends and the impacts of various factors on urbanization. Previous studies have shown that this time frame encompasses significant policy changes and economic development phases in China, which have greatly influenced urban growth patterns [19,20]. By using the remote-sensing processing software ENVI 5.4, we aim to analyze the spatial and temporal variation characteristics of Hefei's land use, urbanization process, urban heat-island effect, and its influencing factors. Figure 1 shows the flow of this study.
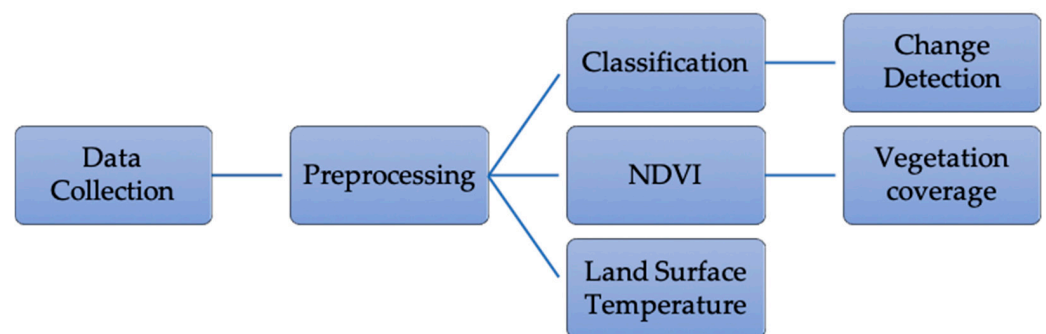

Figure 1. Flow chart of data processing.

2. Data Collection

2.1. Study Area

Hefei is the capital of Anhui Province, China's important research and education base. Hefei is named after the Dongfei River and the Nanfei River. As of the end of 2015, the city's total area is 11,445.1 km^2 (including 770 km^2 of Chaohu Lake), of which the urban built-up area of Hefei's urban area is 403 km^2, and the resident population is 7.79 million, of which the registered population of Hefei's urban area is 2.510 million. Hefei currently has four counties (Feidong, Feixi, Changfeng, and Lujiang), one city (county-level city Chaohu), four

districts (Yaohai, Luyang, Shushan, and Baohe), and four major development zones (Hefei High-Tech Industrial Development Zone, Hefei Economic and Technological Development Zone, Hefei New Station Comprehensive Development Experimental Zone, and Hefei–Chaohu Economic Development Zone). Hefei is located in the mid-latitude zone and belongs to the subtropical monsoon humid climate. The annual average temperature is 15.7 °C, the average annual precipitation is about 1000 mm, and the annual sunshine time is about 2000 h. Chaohu Lake is one of the five largest freshwater lakes in China and has a water area of 770 km^2. It is known as the "eight hundred miles of Chaohu Lake" [21,22]. The geographic location of Hefei is the highlighted area in Figure 2.
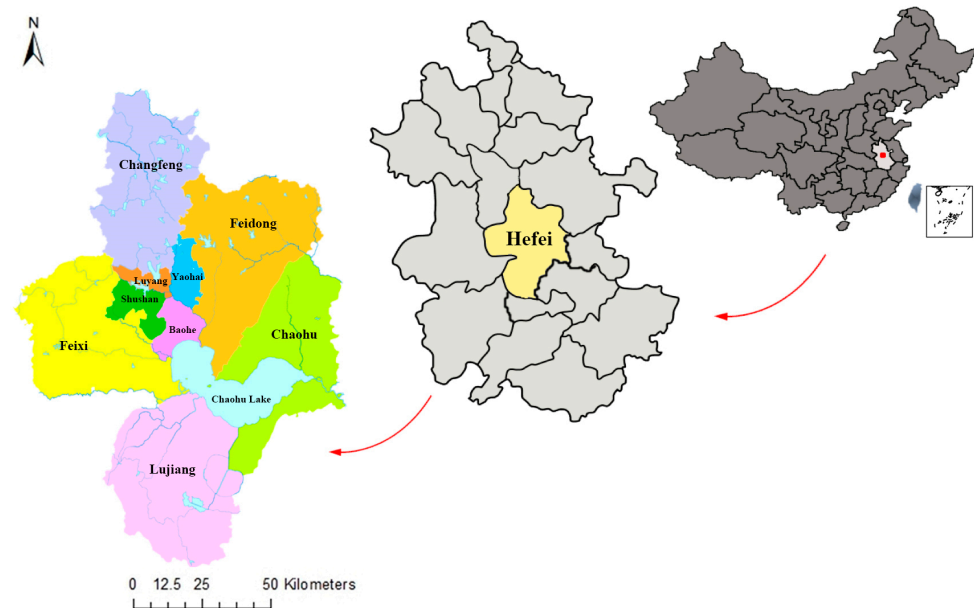

Figure 2. Location of Hefei, Anhui Province.

2.2. Image Data

In this study, image data of Hefei were downloaded from the Geospatial Data Cloud. The data used were Landsat5 TM images in 1995 and 2005, and a Landsat8 OLI image in 2018. The original image has a cloud volume of less than 0.5%. The image is clear, and the data quality is good, which has certain practical significance. Figure 3 shows the original images, which have not been processed, and the colors of the images are represented by true colors.
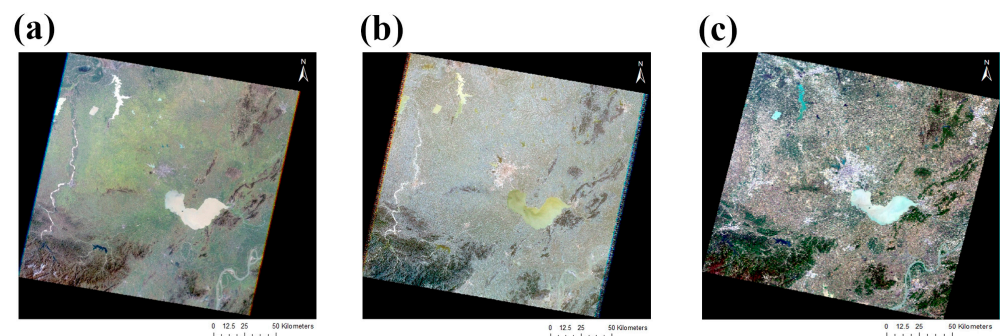

Figure 3. The original images: (**a**) March 1995; (**b**) April 2005; (**c**) April 2018.

The imaging times of the three images were 26 March 1995, 19 April 2005, and 10 April 2018. The imaging time is from March to April, which belongs to the spring in Hefei, and the temperature differences are small. Given the stable nature of land-use types within one year, we only need to utilize image data from a single day. Our study focuses on long-term changes rather than seasonal variations, and the indicators do not

depend on the season. The Landsat5 TM image has seven bands, of which band 6 is the thermal infrared band. The Landsat8 OLI image contains all the bands of the TM image and has been adjusted for some bands, adding a blue wave band for band coast observation (band 1, 0.433–0.453 μm) and a short-wave infrared band (band 9, 1.360–1.390 μm) that includes a strong moisture-absorption feature for cloud detection. Table 1 shows the specific information of the three images.

Table 1. Experimental data collection.

File Name	26 March 1995	19 April 2005	10 April 2018
Location		Hefei	
Sensor	Landsat5 TM	Landsat5 TM	Landsat8 OLI
Spatial		30 m × 30 m	
Temporal	March 1995	April 2005	April 2018
Spectral (micrometers)	Band 1 = Blue (0.45–0.52) Band 2 = Green (0.52–0.6) Band 3 = Red (0.63–0.69) Band 4 = NIR (0.76–0.9) Band 5 = SWIR (1.55–1.75) Band 6 = TIR (10.4–12.5) Band 7 = SWIR (2.08–2.35)	Band 1 = Blue (0.45–0.52) Band 2 = Green (0.52–0.6) Band 3 = Red (0.63–0.69) Band 4 = NIR (0.76–0.9) Band 5 = SWIR (1.55–1.75) Band 6 = TIR (10.4–12.5) Band 7 = SWIR (2.08–2.35)	Band 1 = Coastal (0.433–0.453) Band 2 = Blue (0.450–0.515) Band 3 = Green (0.525–0.6) Band 4 = Red (0.630–0.680) Band 5 = NIR (0.845–0.885) Band 6 = SWIR 1 (1.560–1.660) Band 7 = SWIR 2 (2.100–2.300) Band 8 = Pan (0.500–0.680) Band 9 = Cirrus (1.360–1.390) Band 10 = TIRS 1 (10.6–11.2) Band 11 = TIRS 2 (12.0–12.5)

(Source: http://www.gscloud.cn, accessed on 15 May 2019) [23].

3. Methodology

3.1. Pre-Processing

3.1.1. Radiometric Calibration

Radiometric calibration is a process of converting a voltage or digital quantized value recorded by a sensor into an absolute radiance value or converting it into a relative value related to physical quantities [13]. The radiometric calibration parameters are typically stored in a metadata file. The universal radiometric calibration tool in ENVI automatically reads the parameters from the metadata file to complete the radiometric calibration. The principle of radiometric calibration can be expressed by Formula (1):

$$L = gain \times DN + offset \tag{1}$$

Among them, $gain = \frac{L_{max} - L_{min}}{full\ DN\ range} = \frac{L_{max} - L_{min}}{DN_{max} - DN_{min}}$, $offset = L_{min}$. L is the spectral radiance of a certain band, $gain$ is the incremental correction coefficient, $offset$ is the correction deviation amount, DN is the image gray value, DN_{max} and DN_{min} are the maximum and minimum gray values of the remote sensor, and L_{max} and L_{min} are the radiances corresponding to the maximum and minimum gray values.

3.1.2. Atmospheric Correction

The purpose of atmospheric correction is to eliminate the influence of atmospheric and illumination factors on the reflection of ground objects and obtain real physical model parameters, including the elimination of water vapor, oxygen, carbon dioxide, methane, and ozone in the atmosphere. The effect on the reflection of the ground object also eliminates the effects of atmospheric molecules and aerosol scattering. The principle of atmospheric correction can be expressed by Formula (2) [24]:

$$\rho \times (\theta_s, \theta_v, \varnothing_s) = T_g(\theta_s,\ \theta_v)\left[\rho_{r+a} + T(\theta_s)T(\theta_v)\frac{\rho_s}{1 - S_{\rho_s}}\right] \tag{2}$$

In Formula (2), ρ_{r+a} is the scattering rate of molecular and aerosol scattering, $T_g(\theta_s, \theta_v)$ is the reflectivity of atmospheric absorption, S is the spherical atmospheric reflectivity, and ρ_s is the reflectivity of the target on land. $T(\theta_s)$ is the scattering transmittance of the sun to the ground, and θ_s and θ_v are the elevation angles of the sun and the sensor.

3.2. Land-Use Classification

Maximum likelihood classification is one of the commonly used methods for the supervised classification of remote-sensing images. It is based on the Bayes criterion and focuses on the statistical properties of the cluster distribution [25]. This method assumes that each category of each band in the image is normally distributed. In the process of classification, calculate the probability of each pixel's category and classify the pixels into the category with the highest probability, thus completing the classification of the image [26,27]. The method calculates the global prior probability density function by assuming the spectral characteristics of all the samples obtained in the training area, which is similar to the random phenomenon in nature and is generally subject to normal distribution [25]. The remote-sensing image needed in an experimental study is divided into N categories, where W_η represents the category, x is the pixel to be classified, and the probability of x belonging to one of the categories is calculated. The formula is:

$$P(W_\eta|x), \eta = 1, 2, \ldots, N \tag{3}$$

Then, the method for judging that x belongs to one of the categories is [28]:

$$\forall j(j \neq \eta),\ P(W_\eta|x) > P(W_j|x),\ x \in W_\eta \tag{4}$$

3.3. Dynamic Monitoring

Remote-sensing dynamic monitoring is the quantitative analysis and determination of the characteristics and processes of surface changes from remote-sensing data in different periods [29]. The result comparison method after classification is to classify the remote-sensing images of the two phases that have been registered separately and, then, compare the classification results to obtain the change detection information. Although the accuracy of this method depends on the accuracy of the classification and the consistency of the classification criteria, it is still very effective for practical applications. In the analysis of the expansion of urban space, two parameters were used, namely the urban expansion rate and the average annual expansion rate [30]:

$$V = \frac{A_b - A_a}{t} \tag{5}$$

V represents the urban expansion rate, A_a and A_b represent the urban area at the beginning and end of the study, and t represents the time interval. The intensity of urban expansion is an important indicator reflecting the spatial expansion of urban expansion. By analyzing the intensity of urban expansion, the degree and speed of urban expansion can be quantitatively compared [31]:

$$AGR = \left[\frac{UA_{n+i} - UA_i}{n \times UA_i}\right] \times 100\% \tag{6}$$

AGR represents the urban expansion intensity, UA_{n+i} and UA_i represent the urban area in the $n + i$ and n year, and n represents time. The greater the value of AGR, the faster the urban area expands.

3.4. NDVI and VFC

Vegetation coverage refers to the percentage of the vertical projection area of vegetation on the ground as a percentage of the total area. Vegetation coverage is often used for vegetation change, ecological environment research, soil and water conservation, and climate.

A practical method is to approximate vegetation coverage by using the vegetation index. The commonly used vegetation index is NDVI. NDVI is a numerical value calculated from linear and nonlinear combinations of multispectral data acquired by remote-sensing sensors based on the characteristics of the vegetation reflection band [32]. It has a certain indication significance for vegetation coverage. Generally, the combination of strong absorption of the visible red band and strong reflection of the near-infrared band is used [33,34]. The calculation formula is:

$$NDVI = \frac{D_{NIR} - D_R}{D_{NIR} + D_R} \tag{7}$$

NDVI is between -1 and 1, and the negative value indicates that the ground cover is cloud, water, snow, etc. The visible light is highly reflective. Zero means rock or bare soil, etc. NIR and R are approximately equal. Positive values indicate vegetation coverage and increase with coverage. Vegetation coverage can be expressed as:

$$VFC = \frac{NDVI - NDVI_{soil}}{NDVI_{veg} - NDVI_{soil}} \tag{8}$$

This area approximates $NDVI_{max}$ and $NDVI_{min}$ as $NDVI_{veg}$ and $NDVI_{soil}$, which gives:

$$VFC = \frac{NDVI - NDVI_{min}}{NDVI_{max} - NDVI_{min}} \tag{9}$$

Due to the inevitable noise in the image, the extremum of NDVI is not necessarily $NDVI_{max}$ and $NDVI_{min}$. Therefore, when this value is taken, it does not directly take the maximum and minimum values of NDVI in the region but instead takes the given maximum and minimum values within the confidence interval [35]. The value of confidence is mainly determined by the image size, image clarity, and so on.

3.5. Land Surface Temperature

In this study, the surface temperature is retrieved based on the atmospheric correction method. First, the influence of the atmosphere on the surface's thermal radiation is estimated, and then, this part of the atmospheric influence is subtracted from the total amount of thermal radiation observed by the satellite sensor to obtain the surface thermal radiation intensity. Then, the thermal radiation intensity is converted into the corresponding surface temperature. The thermal infrared band radiant energy (luminance value) L_λ received by the satellite sensor consists of three parts: atmospheric direct thermal radiation $L_\uparrow$, atmospheric thermal radiation to the ground $L_\downarrow$, and the true radiant brightness of the ground received by the satellite sensor after being attenuated by the atmosphere. Assuming that the surface and atmosphere have a Lambertian property for thermal radiation [36], according to the radiation conduction equation, the formula of the radiance L_T of the black body in the thermal infrared band with the same real temperature as the surface can be derived:

$$L_T = \left(L_\lambda - L_\uparrow - \tau(1 - \varepsilon)L_\downarrow\right)\tau\varepsilon \tag{10}$$

In Formula (10), ε is the surface-specific emissivity, transmittance τ, atmospheric direct thermal radiation $L_\uparrow$, and atmospheric thermal radiation to the ground $L_\downarrow$. These three parameters can be found on the NASA official website (http://www.usgs.gov, accessed on 15 May 2019) [37]. Then, we need to input the image imaging time, center latitude and longitude, relevant area pressure, and other related information. Since the site only records data after 2000, only the surface temperatures of 2005 and 2018 are inverted here. According to the inverse function of the Planck formula, the formula for calculating the true temperature of the surface is derived:

$$T = K_2 / ln\left(\frac{K_1}{L_T} + 1\right) \tag{11}$$

Among them, K_1 and K_2 are constants. For the TM images, K_1 = 607.76 W/(m²·μm·sr), and K_2 = 1260.56 K. For band 10 of the OLI images, K_1 = 774.89 W/(m²·μm·sr), and K_2 = 1321.08 K [38]. The surface temperature is normalized for easy comparison. The formula is as follows:

$$N = \frac{T - T_{min}}{T_{max} - T_{min}} \qquad (12)$$

where N represents the temperature's normalized value, T represents the surface temperature, T_{min} represents the minimum value of the surface temperature in the image, and T_{max} represents the maximum value of the surface temperature in the image. The maximum and minimum values here take the maximum value T_{max} (97%) and the minimum value T_{min} (3%) within a given confidence interval.

4. Experiment

4.1. Pre-Processing

The data for 1995 and 2005 come from the Landsat5 TM sensor, and the data for 2018 come from the Landsat8 OLI sensor. Since the data are sourced from different sensors or the same sensor at different time periods, some data need to be pre-processed for convenient comparison. The parameters for radiometric calibration are generally stored in a metadata file, and a general radiometric calibration tool in ENVI can be used directly. Use this method for atmospheric correction after setting parameters such as the date. Figure 4 is the image after pre-processing.
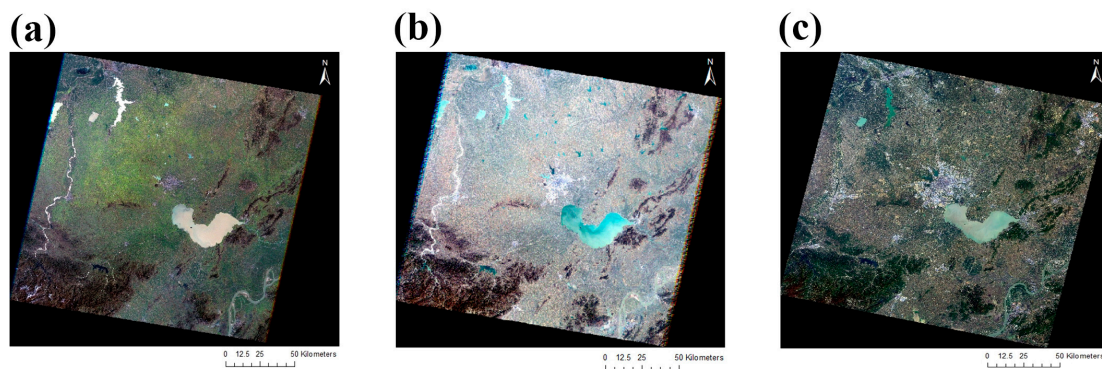

(a) **(b)** **(c)**

Figure 4. The preprocessing results for 1995 (**a**), 2005 (**b**), and 2018 (**c**).

4.2. Land-Use Analysis

4.2.1. Classification

After the vector is cropped, the TM image is synthesized into RGB in bands 3, 2, and 1 to simulate the true color image. The OLI image is displayed in RGB in bands 4, 3, and 2. According to the spectral characteristics of the image, four supervised classification sample regions are created by manual judgment, and the features in the image are divided into four categories: construction land, vegetation, water, and other (cultivated land). By drawing the polygonal region of interest and selecting the sample, the regions of interest for each type of land are distinguished by different colors. The above four types of features are represented by red, green, blue, and yellow. Then, calculate the separability of the sample; the standard value of the separation of the selected samples is improved on the premise of ensuring the reliability of the sample data [39]. Finally, by looking at the report, it is found that the standard value of the sample's separability is between 1.7 and 1.9, which is in the range of good separation. The larger the value, the better the separability between the samples. In this study, select the Maximum Likelihood Classification in Toolbox to perform supervised classification. The classification results are shown in Figure 5. The trend of urban expansion is obvious, especially the expansion in the southwest direction of the main city. Four counties in Hefei and Chaohu City in the east also have a certain degree of expansion.
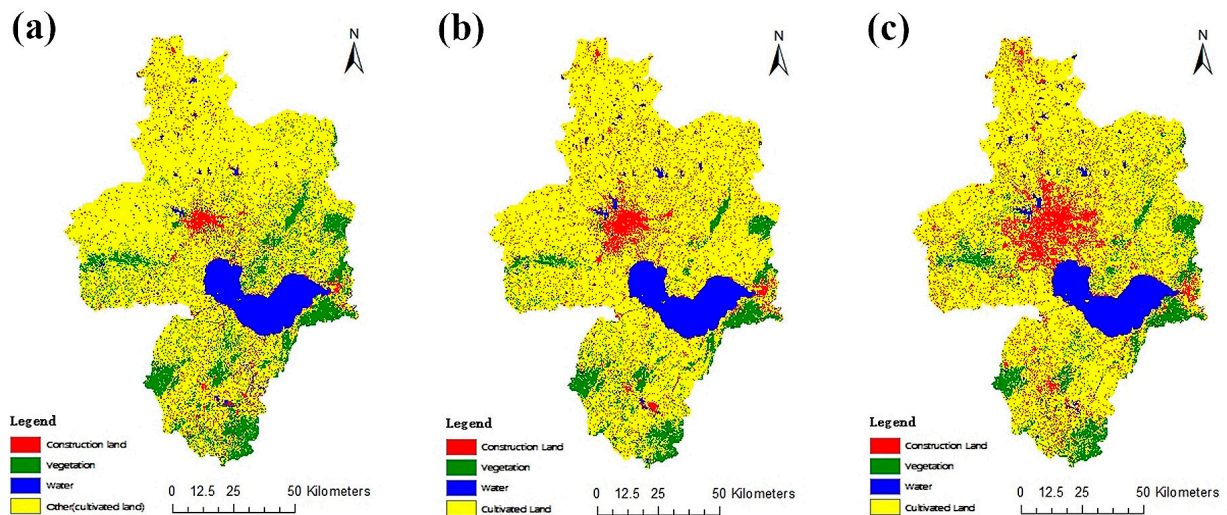
Figure 5. Land use of Hefei in 1995 (**a**), 2005 (**b**), and 2018 (**c**).

4.2.2. Confusion Matrix

In ENVI 5.1, we used the confusion matrix calculation tool from the toolbox to calculate the confusion matrix using ground-truth ROIs. The software automatically matches according to the classification code to generate an accuracy report. As displayed in Table 2, the supervised classification accuracies for the years 1995, 2005, and 2018 are relatively high and hold significant reference value.

Table 2. Land use classification accuracy.

	1995	2005	2018
Overall Accuracy	84.97%	81.25%	88.65%
Kappa Coefficient	0.803	0.749	0.836

4.3. Change Detection

4.3.1. Majority/Minority Analysis

When applying supervised classification, it is inevitable that some small area patches will be generated in the classification results. These small patches need to be removed or reclassified for better thematic mapping and practical application. In this study, we used the Majority/Minority analysis tool to address this issue. This tool helps refine the classification results by removing small patches, making it more convenient to analyze the expansion of urban construction land, as shown in Figure 6. By focusing on the area within a 20 km radius centered on the city center, we were able to study the changes in the downtown area of Hefei more effectively.

4.3.2. Thematic Change Workflow

Use the process tool Thematic Change Workflow in ENVI for post-classification comparisons. In the Toolbox, open Thematic Change Workflow and select "Only Include Areas That Have Changed" to get only the area where the construction land changes. As shown in Figure 7, it is found that from 1995 to 2018, the urban construction land area of Hefei's downtown area was getting larger and larger in three different time periods. The expansion of the area of the built-up area has brought about a significant change in the urban form. It has entered the expansion period of the dispersed group by the extension period along the transportation line. The construction of various economic development zones and industrial parks has transformed the urban form from the central city to the group-based city [7], and the city's center of gravity shifts to the south and west. With the completion of

the Hefei Economic and Technological Development Zone, the Hefei Municipal New District, and the Shushan New Industrial Park, especially the development of the Binhu New District, the construction land of Hefei has expanded significantly to the west and south.
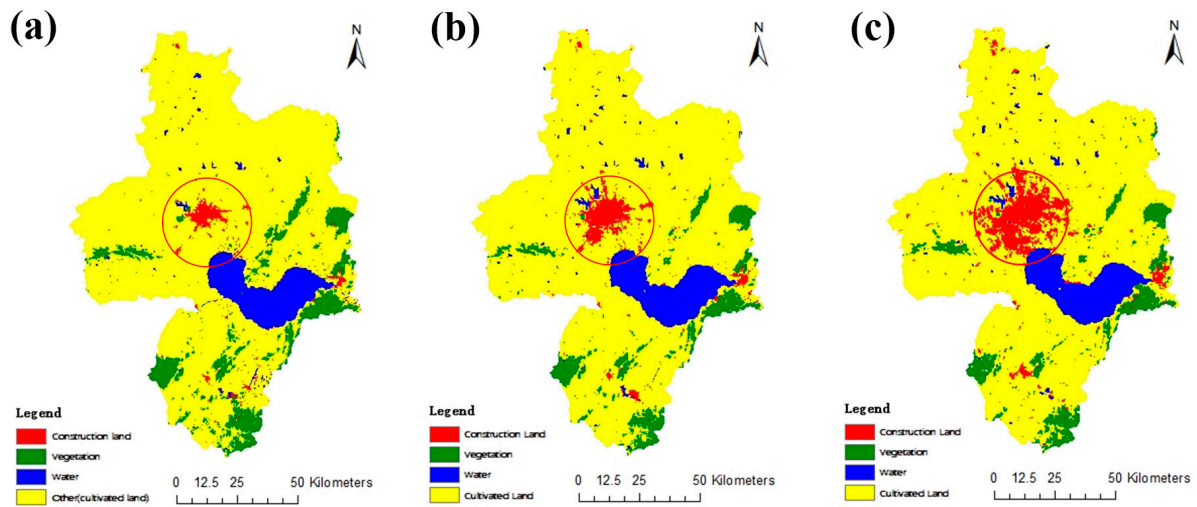

Figure 6. Majority/Minority analysis of Hefei in 1995 (**a**), 2005 (**b**), and 2018 (**c**). Red circle: the downtown area of Hefei.
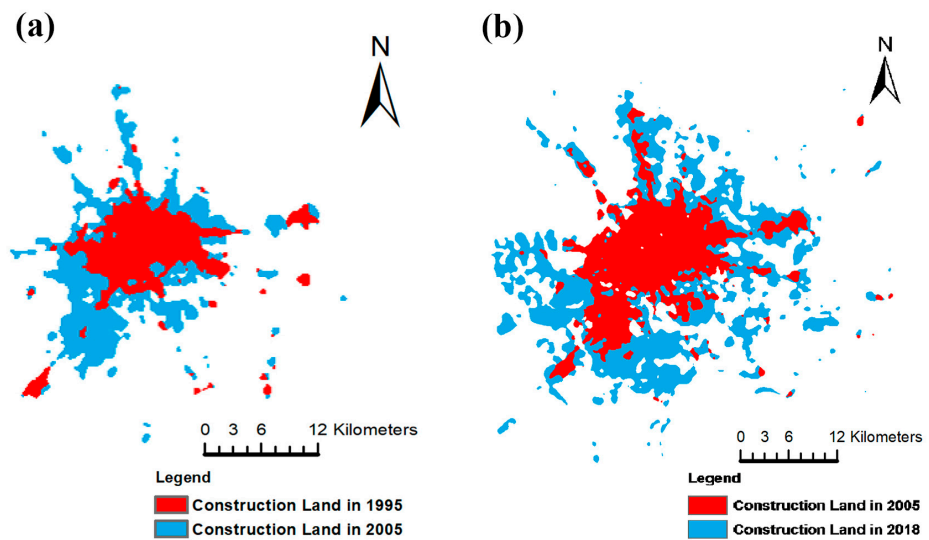

Figure 7. Expansion of construction land from 1995 to 2005 (**a**) and 2005 to 2018 (**b**).

4.4. Vegetation Coverage Analysis

In ENVI 5.1, select NDVI in Transform and use the preprocessed image to calculate NDVI. Select Compute Statistics to create a mask file using the ROI generated by the vector data of Hefei in the file selection dialog. In the statistical results, NDVI values with cumulative probabilities of 5% and 95% were taken as $NDVI_{min}$ and $NDVI_{max}$. Here, it is in Table 3:

Table 3. Confidence interval of NDVI.

Confidence Interval	April 2005	April 2018
$NDVI_{min}$ (5%)	−0.442	−0.475
$NDVI_{max}$ (95%)	0.174	0.788

Vegetation coverage is calculated using Band Math. Select Density Slice and add 10 intervals in turn to get the vegetation coverage map for 2005 and 2018. As shown in Figure 8, the spatial distribution characteristics of vegetation coverage in Hefei are centered on the main urban area. The part with low vegetation coverage is mainly the main urban area of Hefei, and the surrounding vegetation coverage is high. With the expansion of the city, the area with low vegetation coverage around the main urban area is expanding, and the area with an obvious reduction in vegetation area is an area with active economic development. By comparison, the overall vegetation coverage of Hefei in 2018 is significantly higher than that in 2005, especially the reconstruction of Dashushan National Forest Park in the west of Hefei, about 10 km away from the downtown area of Hefei, and the construction of the Zipengshan National Forest Park in Feixi County has significantly increased the amount of vegetation in the west and south of Hefei.
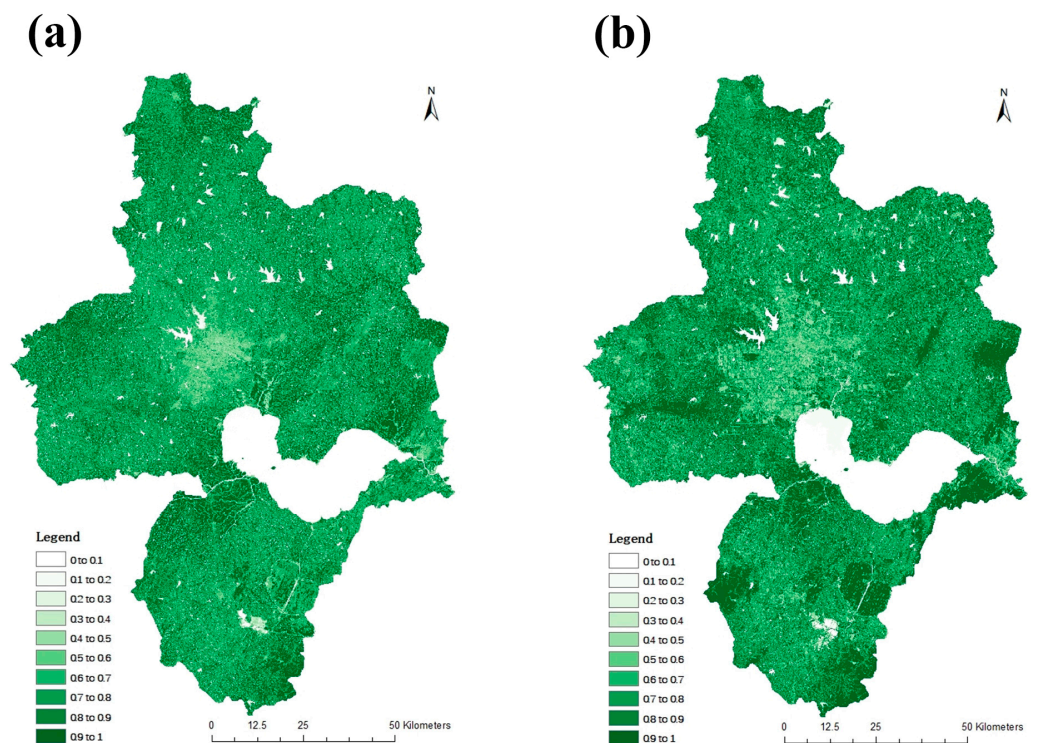
(a) **(b)**

Figure 8. Vegetation coverage in 2005 (**a**) and 2018 (**b**).

4.5. Land Surface Temperature Retrieval

4.5.1. Retrieval of Land Surface Temperature

In the Toolbox, select Radiometric Calibration to output the radiance image of the thermal infrared band. The thermal infrared band uses band 6 of the Landsat5 TM image in 2005 and band 10 of the Landsat8 OLI image in 2018. In the Toolbox, select Band Math to calculate surface-specific emissivity, blackbody radiance, and surface temperature. In ArcGIS, the color gradient is set for the image of the surface temperature.

As displayed in Figure 9, in 2005, the surface temperature of the main urban area of Hefei was very high, and the high-temperature area was concentrated. The heat-island effect in the main urban area and Chaohu City in the east was remarkable. In 2018, the range of the heat-island effect in the main urban and suburban counties continued to expand, but the intensity declined.
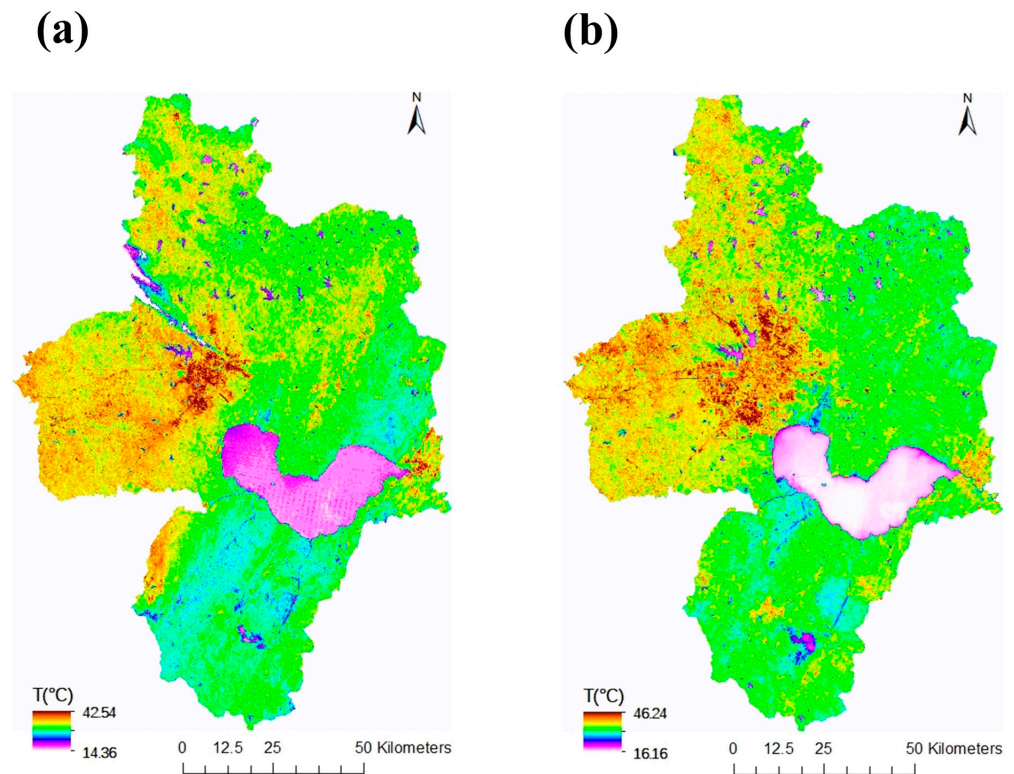
(a)   **(b)**

Figure 9. Retrieval of land surface temperature in 2005 (**a**) and 2018 (**b**).

4.5.2. Raster Normalization

Since the imaging time of the images used is different, it is obviously unreasonable to directly compare the inversion temperatures. In order to eliminate the influence of time, this paper normalizes the obtained surface temperature and unifies the temperature range of the two periods to between zero and one. In the statistical results, the surface temperature values with cumulative probabilities of 3% and 97% were taken as T_{min} and T_{max}. Here it is in Table 4:

Table 4. Confidence interval of surface temperature.

Confidence Interval	April 2005	April 2018
T_{min} (3%)	17.211 °C	16.783 °C
T_{max} (97%)	26.501 °C	32.642 °C

As shown in Figure 10, the normalized surface temperature is divided into five grades. In 2005, the built-up area of the city was fiery red, and the strip-shaped radiation along the traffic line also displayed a distinct red color. Hefei's construction land expanded rapidly since 2005, and so does Hefei's heat island, which displayed a multi-center, fragmented pattern in 2018. In addition to the old towns located in the Yaohai District and Luyang District, the Shushan New Industrial Park, the Hefei Municipal New District, Binhu New District, the Economic and Technological Development Zone, and the Baohe Industrial Park began to demonstrate high-temperature zones and extremely high-temperature zones. However, the intensity of the heat-island effect in the old city somewhat weakened, and some high-temperature areas converted into sub-high-temperature zones and medium-temperature zones. What is more, located in the southeast of Hefei, Chaohu Lake, which is one of the five freshwater lakes in China, regulates the microclimate of the surroundings effectively with its water coverage of about 760 km². By means of evaporation, it absorbs heat and, consequently, reduces temperature in adjacent areas. It can be seen from Figure 10

that, in recent years, with the continuous increase in the urban temperature, the climate-regulating ability of Chaohu Lake has been weakened, and some sub-low-temperature regions around the lake have gradually changed to medium-temperature regions. In addition, the Dongpu Reservoir and the Dafangying Reservoir in the northwestern part of the downtown area have lower average temperatures and also play a role in regulating the temperature around them.
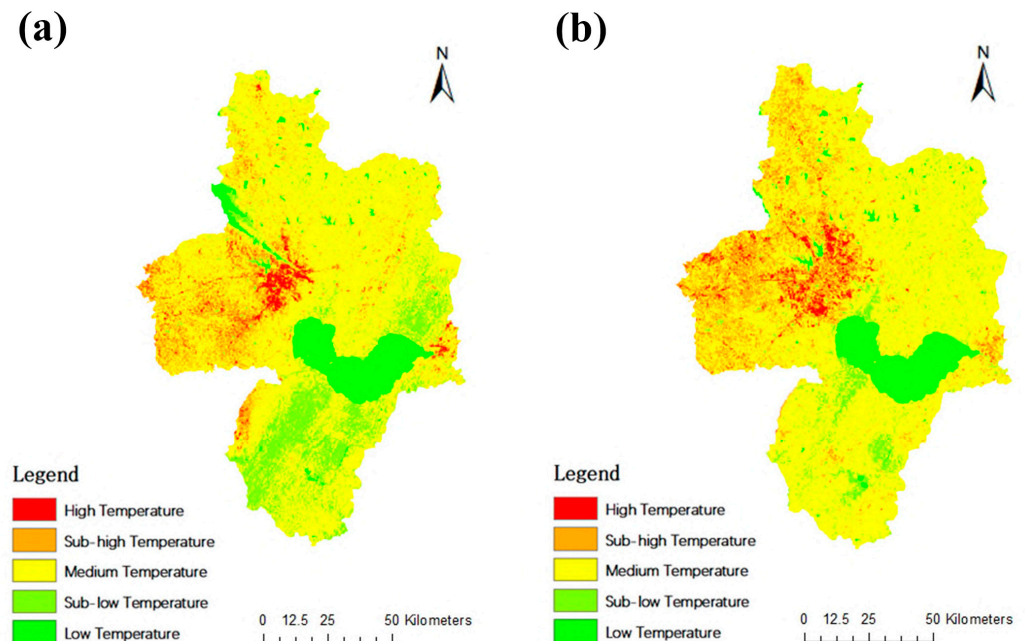

Figure 10. Normalized surface temperature in 2005 (**a**) and 2018 (**b**).

5. Results and Analysis

5.1. Land-Use and Land-Cover Change

The land-use classifications for the three years are counted to obtain the area of each land-use type for each year. As shown in Table 5, the construction land has expanded from 719.032 km^2 in 1995 to 1518.418 km^2 in 2018, and the expansion area has more than doubled. This shows that the urbanization process of Hefei has developed rapidly during these 20 years. This may be related to the construction of the city in Hefei in the early 21st century; a large amount of undeveloped land is used to build cities. The area of vegetation has been reduced slightly, and the area of water has increased. Combined with Figure 5, this may be due to the construction of the Dafangying Reservoir.

Table 5. Area of each land-use type in each year.

Year	Construction Land	Vegetation	Water	Other
1995	719.032 km^2	1605.210 km^2	699.452 km^2	8396.535 km^2
2005	1081.202 km^2	1385.600 km^2	916.329 km^2	8037.095 km^2
2018	1518.418 km^2	1149.689 km^2	902.601 km^2	7849.529 km^2

The percentage of land-use area in each year as a percentage of the total area is counted as shown in Figure 11. The undeveloped land (Other) includes areas not yet utilized for specific purposes and has always been the main land-use type. Vegetation refers to forests and green spaces. Construction land represents areas developed for urban infrastructure, buildings, and roads, which have continued to rise in proportion, and water areas include lakes, rivers, and reservoirs. In 1995 and 2005, the percentage of land use in Hefei was: Other > Vegetation > Construction Land > Water. By 2018, the order

changed to Other > Construction Land > Vegetation > Water. Notably, in 2018, construction land surpassed vegetation, becoming the second largest land-use type after undeveloped land, with its proportion reaching 13%. This shift highlights the rapid urbanization and infrastructure development in Hefei over the past decades.
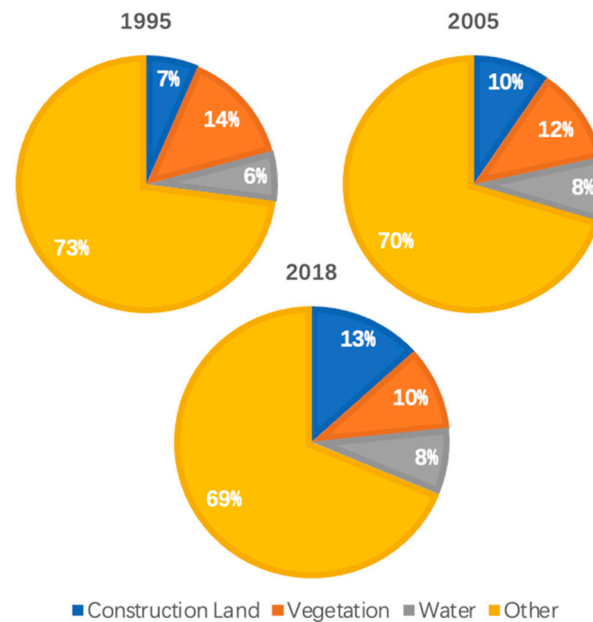

Figure 11. Percentage of land-use area in each year.

5.2. Analysis of Construction Land Expansion

Table 6 shows the construction land changes in the downtown area of Hefei. In 2005, construction land expanded to 343.823 km^2, with 49.143% converted from other land use, including small amounts of vegetation and water. In 2018, it expanded to 802.496 km^2, with 54.704% converted from other land use. Each decade, the area converted to construction land exceeds the original construction land area, indicating significant urban changes.

Table 6. Changes in construction land.

Year	Original Construction Land	"Vegetation" to "Construction Land"	"Water" to "Construction Land"	"Other" to "Construction Land"	Total Construction Land
1995 to 2005	161.105 km^2 (46.857%)	9.003 km^2 (2.618%)	4.752 km^2 (1.382%)	168.963 km^2 (49.143%)	343.823 km^2
2005 to 2018	343.823 km^2 (42.844%)	5.823 km^2 (0.726%)	13.852 km^2 (1.726%)	438.998 km^2 (54.704%)	802.496 km^2

To better understand the dynamics of urban expansion in Hefei, we calculated the urban expansion rate and urban expansion intensity using Formulas (5) and (6). Table 7 shows that the overall urban expansion rate in Hefei over the past 20 years has been relatively fast, particularly between 2005 and 2018. From 1995 to 2005, the annual expansion rate was 18.272 km^2, which accelerated to an average annual rate of 35.283 km^2 from 2005 to 2018. This rapid growth rate underscores the significant transformation of the urban landscape in Hefei.

Moreover, comparing the intensity of urban expansion across different periods can provide insights into the scale characteristics of this expansion. From 1995 to 2005, the urban expansion intensity index was 11.342% and increased to 12.262% from 2005 to 2018. These figures suggest that Hefei's urban expansion is at a medium level overall but has been intensifying year by year.

Table 7. Urban expansion rate and urban expansion intensity.

Year	V (Urban Expansion Rate)	AGR (Urban Expansion Intensity)
1995 to 2005	18.272 (km^2/year)	11.342%
2005 to 2018	35.283 (km^2/year)	12.262%
1995 to 2018	27.887 (km^2/year)	17.310%

These findings align with the broader patterns observed in other rapidly developing cities in China. For instance, Wang et al. analyzed the urban heat-island effect in Shanghai and found that land-use and land-cover changes significantly contribute to urban ecological and environmental issues, with impervious surfaces playing a crucial role [24]. Similarly, Wong et al. assessed impervious surface changes in Hong Kong, highlighting the challenges of high-density urban development and its environmental implications [17]. An et al. studied land-use changes in Hangzhou, revealing substantial rural-to-urban transformation over recent decades driven by rapid urbanization policies [19]. These studies underscore the importance of understanding the interplay between urban expansion, land-use policies, and environmental impacts. Our findings contribute to this body of knowledge by providing a detailed case study of Hefei's urban expansion dynamics, emphasizing the need for sustainable urban planning and management strategies.

5.3. Drivers of Urban Expansion

5.3.1. Natural Geography

The natural environment is the foundation of urban expansion and the guarantee of urban economic development [7]. For Hefei, there is an extinct volcano in the west, two large reservoirs in the northwest, and Chaohu Lake in the south. These natural environments limit the expansion of the city. In addition, the north and east of Hefei are bordered by counties and districts, and the development space is also limited. Only in the southwestern part of the city is the terrain flat, open, and with good geological and hydrological conditions, which are most suitable as the main development direction of the city [40]. This is also a good explanation of the reasons for the development of Binhu New District.

5.3.2. Economic Development

Since the reform and opening up, Hefei's economic development has entered a new stage. GDP has been rising, and the city's economic strength has been continuously enhanced. Figure 12 shows the GDP of Hefei from 1995 to 2018. Hefei's GDP showed a rapid growth trend, with GDP reaching 7822.91 billion. This has not only become a strong proof of Hefei's economic development but has also laid a solid economic foundation for its urban expansion. It can be seen that, with the development of the economy, urban expansion is an inevitable trend in Hefei.

5.3.3. Population Growth

Population is the main factor of urban composition [42]. Hefei, as the capital of Anhui Province, was developed on the basis of being a small city, and with the advancement of the national urbanization policy and the growing economy, the number of permanent residents in Hefei is increasing. Figure 13 shows the resident population of Hefei from 1995 to 2018. The amount of urban population in Hefei has been increasing, reaching 4.26 million by the end of 2018, and the trend of urbanization has accelerated significantly since 2010. This is mainly due to the economic construction of Hefei, which has led to a large amount of surplus rural labor in the city, and the expansion of the city will gradually transform the rural agricultural population into an urban population. In addition, the well-off rural population has moved into cities, and the vast majority of university

graduates remain in cities. Due to these demographic factors, the area of construction land is constantly expanding.
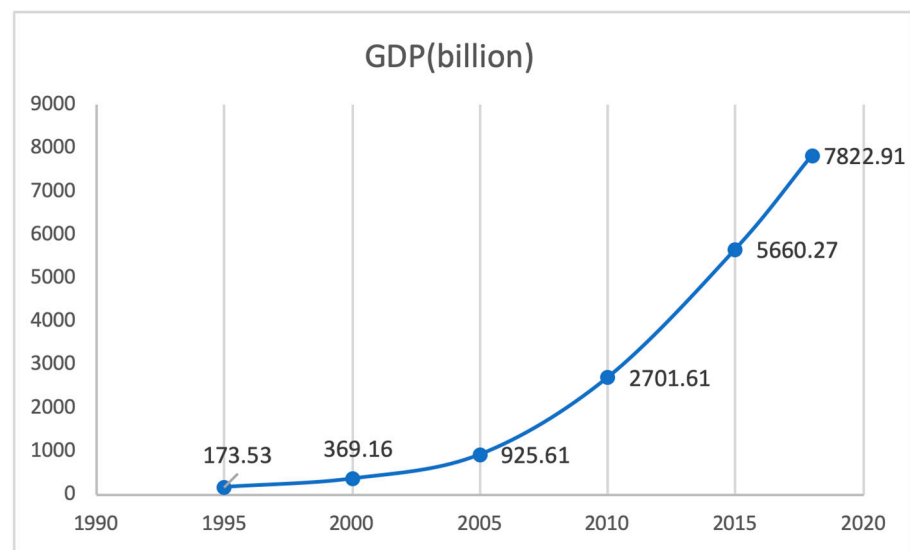

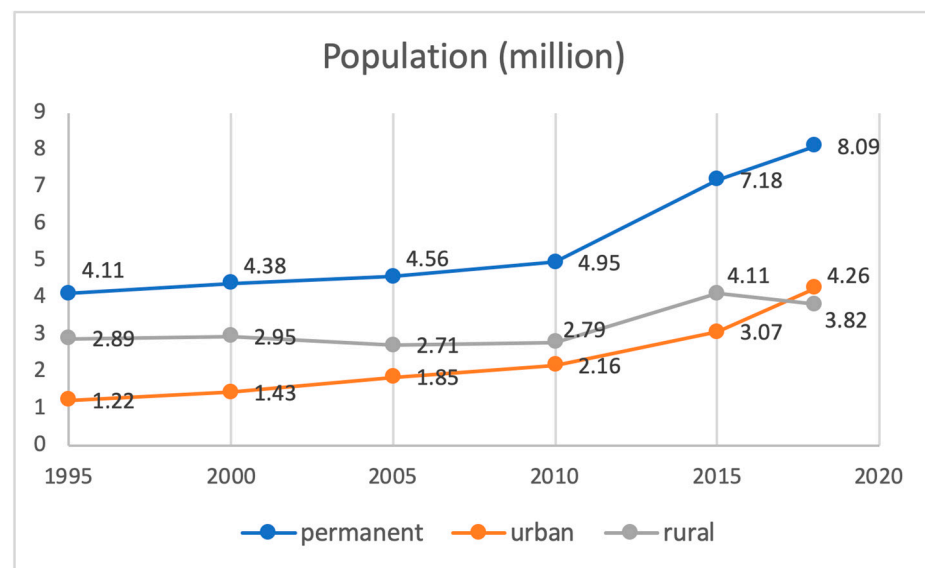**Figure 12.** The change of GDP in Hefei in recent years. (Source: http://tjj.hefei.gov.cn, accessed on 15 May 2019) [41].

Figure 13. The resident population in Hefei. (Source: http://tjj.hefei.gov.cn, accessed on 15 May 2019) [41].

5.3.4. Government Policy

In 1992, after Hefei was designated as an open-up city, the municipal government set up the strategic goal of "open development and re-engineering of the new Hefei", which contributed to the accelerated expansion of the city. In addition, in order to strengthen the construction of the Binhu New District, the government put forward the "141" space development strategy. It is pointed out that Hefei should be built into a "one main city, four groups, one lakeside new area" model [43]. This makes Hefei's expansion mode change from the original "ring expansion" to southwest development [44].

5.4. Analysis of Vegetation Coverage

The distribution of vegetation coverage in 2005 and 2018 is calculated and divided into five categories. As can be seen from Table 8, in 2005, the largest proportion was sub-high vegetation coverage, reaching 49.139%. In 2018, the largest proportion was the high vegetation coverage, which reached 39.632%. The proportion of sub-high vegetation coverage decreased from 2005 to 2018, and the proportion of medium vegetation coverage and high vegetation coverage is increasing.

Table 8. Distribution of vegetation coverage in each grade.

VFC Grade	April 2005	April 2018
Low Vegetation Coverage (0 to 0.2)	8.326%	8.091%
Sub-low Vegetation Coverage (0.2 to 0.4)	1.864%	1.752%
Medium Vegetation Coverage (0.4 to 0.6)	8.874%	10.740%
Sub-high Vegetation Coverage (0.6 to 0.8)	49.139%	39.785%
High Vegetation Coverage (0.8 to 1.0)	31.797%	39.632%

The changing rate of vegetation coverage in Hefei from 2005 to 2018 is calculated from Table 8. The results are shown in Table 9. The percentage of sub-high vegetation coverage decreased by 9.354%, the area of low vegetation coverage and sub-low vegetation coverage decreased slightly, and the high vegetation coverage area experienced an apparent increase. This is the result of focusing on ecological environment construction in the rapid expansion of Hefei.

Table 9. The changing rate of vegetation coverage.

VFC Grade	2005 to 2018
Low Vegetation Coverage (0 to 0.2)	−0.235%
Sub-low Vegetation Coverage (0.2 to 0.4)	−0.112%
Medium Vegetation Coverage (0.4 to 0.6)	1.866%
Sub-high Vegetation Coverage (0.6 to 0.8)	−9.354%
High Vegetation Coverage (0.8 to 1.0)	7.835%

5.5. Analysis of Heat-Island Effect

The distribution of surface temperature in April 2005 and April 2018 is statistically analyzed. The results are shown in Tables 10 and 11. In 2005, the surface temperature in the area of 24~26 °C accounted for the largest proportion, reaching 37.105%. In 2018, the surface temperature in the region of 26~28 °C accounted for the largest proportion, reaching 31.122%. It is worth noting that, in 2018, the area of more than 30 °C reached 18.832%, while the area of more than 26 °C in 2005 only accounted for 4.999%.

Table 10. Surface temperature distribution in 2005.

Range (°C)	Percent (%)
Less than 20	8.658
20 to 22	13.645
22 to 24	35.593
24 to 26	37.105
More than 26	4.999

Table 11. Surface temperature distribution in 2018.

Range (°C)	Percent (%)
Less than 24	10.105
24 to 26	12.569
26 to 28	31.122
28 to 30	27.372
More than 30	18.832

The maximum, minimum, and average values of surface temperature in 2005 and 2018 are calculated separately. As shown in Table 12, T_{min}, T_{max}, and T_{mean} in 2018 are higher than the same period in 2005. The historical temperatures of these two dates are queried on https://en.tutiempo.net [45]. Most of the surface temperature retrieval results in this experiment are in this interval, so the retrieval results have a certain reference value.

Table 12. T_{min}, T_{max}, and T_{mean}.

Time	T_{min}	T_{max}	T_{mean}
19 April 2005	14.368 °C	42.545 °C	23.460 °C
10 April 2018	16.162 °C	46.243 °C	27.487 °C

The results of the surface temperature retrieval are normalized and divided into five categories, as displayed in Table 13. In 2005, the sub-high-temperature area was the largest, accounting for 46.291% of the total area. In 2018, the area of the sub-high-temperature area was still the largest, accounting for 48.952%. The high-temperature area increased from 20.818% to 26.518% in 2018. The average values of normalized surface temperatures in 2005 and 2018 were 0.632 and 0.673, both of which belonged to the sub-high-temperature area. The average temperature rose slightly, so vegetation has alleviated the increase in temperature to some extent. The range of high-temperature areas in Hefei was expanding, and the intensity of the heat-island effect has increased in the past 15 years. Combined with Figure 10 for analysis, it is not difficult to see that, except for the water coverage area and the high density of green space and forest, the city basically belonged to the sub-high-temperature and high-temperature areas, and the whole city was fiery red.

Table 13 is used to calculate the changing rate of the surface temperature from 2005 to 2018. The result is displayed in Table 14. From 2005 to 2018, the high-temperature area has increased by 5.7%, and with the acceleration of urbanization, the heat-island effect is becoming more and more significant.

5.6. LST and VFC

The selection of 30 sample points is based on a stratified random sampling method to ensure representative coverage across the study area. These points are chosen from the normalized VFC and LST for the years 2005 and 2018. The sampling strategy ensures

that the points are evenly distributed across different vegetation coverage levels and temperature gradients. To achieve this, the study area was divided into several strata based on VFC values, and sample points were randomly selected within each stratum to capture the variability in both vegetation cover and surface temperature. This method helps in minimizing sampling bias and provides a comprehensive understanding of the relationship between VFC and LST.

Table 13. Distribution of surface temperature in each grade.

LST Grade	April 2005	April 2018
Low Temperature (0 to 0.2)	8.201%	7.282%
Sub-low Temperature (0.2 to 0.4)	2.172%	1.514%
Medium Temperature (0.4 to 0.6)	22.518%	15.734%
Sub-high Temperature (0.6 to 0.8)	46.291%	48.952%
High Temperature (0.8 to 1.0)	20.818%	26.518%
Mean	0.632	0.673

Table 14. The changing rate of surface temperature.

LST Grade	2005 to 2018
Low Temperature (0 to 0.2)	−0.919%
Sub-low Temperature (0.2 to 0.4)	−0.658%
Medium Temperature (0.4 to 0.6)	−6.784%
Sub-high Temperature (0.6 to 0.8)	2.661%
High Temperature (0.8 to 1.0)	5.7%

Figure 14 presents the distribution of these sample points and their corresponding VFC and LST values. A linear fitting analysis was performed on LST (*y*-axis) and VFC (*x*-axis), revealing a significant negative correlation. As shown in the figure, areas with lower VFC tend to have higher surface temperatures, indicating that vegetation coverage plays a crucial role in regulating land surface temperature. This approach ensures that the selected sample points accurately represent the study area's diverse environmental conditions, thereby strengthening the validity of the observed correlation between VFC and LST.

Figures 8 and 10 have revealed that, while the VFC in the urban fringe area is significantly higher than that of the urban center, the LST in the urban fringe area is much lower than that of the urban center. The water surface is a special case. The values of VFC and LST in the Dongpu Reservoir, Dafangying Reservoir in the northwest of Hefei, and Chaohu Lake in the south of Hefei tend to be the lowest. This is because the influence of vegetation on the surface radiant temperature mainly comes from the change of the heat storage structure of the underlying surface and the evapotranspiration. The urban surface lacking vegetation coverage has a high thermal conductivity and a high heat capacity due to the dry nature of the underlying surface without evaporation and transpiration [46,47]. In view

of the opposite relationship between vegetation coverage and land surface temperature, it can be concluded that green vegetation within the city plays a significant role in mitigating the urban heat-island effect. Therefore, rational planning and increasing urban green space are effective measures to alleviate the heat-island effect.
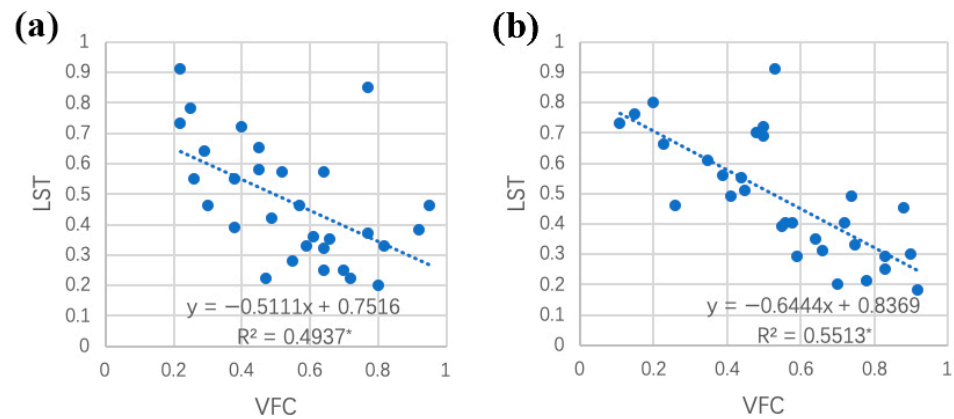

Figure 14. Linear fitting analysis of LST and VFC in 2005 (**a**), and 2018 (**b**). * represents statistical significance at 95% confidence level.

6. Conclusions

In this study, we focused on Hefei as our research area. We conducted pre-processing of remote sensing images from 1995, 2005, and 2018. Supervised classification was performed to categorize land into four types and determine their distribution. Changes in urban land were dynamically monitored to assess urban development patterns in Hefei. We analyzed the rate and intensity of urban expansion, considering natural factors, economic growth, population dynamics, and policy influences. Our analysis of vegetation coverage revealed an expanding area of low vegetation around the urban core. Surface temperature retrieval highlighted a continuous increase in the heat-island area, showing a fragmented, multi-center distribution pattern. As urban development extends into suburban areas, the severity of the heat-island effect intensifies. Linear regression analysis demonstrated an inverse relationship between vegetation coverage and land surface temperature, suggesting vegetation's potential to effectively mitigate the heat-island effect in Hefei.

Remote-sensing retrieval methods offer several distinct advantages. They provide higher spatial resolution, offering finer spatial details compared to standard products. Additionally, these methods improve temporal resolution by enabling more frequent updates and observations, which are essential for dynamic environmental monitoring. Enhanced accuracy is achieved through the integration of multiple data sources and advanced algorithms, which are particularly beneficial in complex terrain or urban areas where precise temperature estimations are critical. Moreover, these methods allow users to customize parameters, adjusting retrieval algorithms to specific research or application needs, thus enhancing flexibility in data interpretation. In this study, remote-sensing retrieval played a crucial role in providing spatial data on land surface temperatures, facilitating the identification of heat-island patterns and their multi-center distribution across Hefei. This technology underscored the significant role of vegetation in mitigating the urban heat-island effect, emphasizing its cooling impact on local temperatures.

In conclusion, this study underscores the significance of remote-sensing retrieval in providing the spatial data that are essential for urban planning and environmental management. By leveraging remote-sensing technology, we not only enhanced our understanding of urban expansion dynamics and heat-island phenomena in Hefei but also emphasized the importance of integrating green infrastructure into urban development strategies. Our policy recommendations emphasize that local authorities in Hefei should prioritize expanding green infrastructure, especially in areas with insufficient vegetation coverage, to effectively mitigate the urban heat-island effect. Additionally, integrating remote-sensing

technologies into urban-planning frameworks can empower planners with precise insights into urban development dynamics and heat-island patterns, thereby facilitating informed decision-making. Finally, we advocate for community engagement and public awareness campaigns to promote the benefits of urban green spaces. Engaging residents in the up-keep and expansion of urban greenery has the potential to bolster local resilience to heat stress and foster a more livable urban environment overall. Implementing these measures will mitigate the adverse effects of urban expansion, improve urban livability, and foster sustainable development in Hefei.

Institutional Review Board Statement: Not applicable.

Informed Consent Statement: Not applicable.

Data Availability Statement: Data are contained within the article.

Conflicts of Interest: The authors declare no conflicts of interest.

References

1. Florida, R.; Adler, P.; Mellander, C. The city as innovation machine. *Reg. Stud.* **2017**, *511*, 86–96. [CrossRef]
2. Friedmann, J. Four theses in the study of China's urbanization. *Int. J. Urban Reg. Res.* **2006**, *302*, 440–451. [CrossRef]
3. Institute of Urban Environment. Available online: http://www.iue.cas.cn (accessed on 15 May 2019).
4. Chen, M.X.; Lu, D.D.; Zhang, H. Comprehensive measurement of China's urbanization level and its dynamic factor analysis. *Geogr. J.* **2009**, *4*, 387–398.
5. Qian, Z.S.; Liu, T.; Wang, X.H.; Dai, Y.; Baninla, J.; Nakatani, Y. Urbanization impacts on greenhouse gas (GHG) emissions of the water infrastructure in China: Trade-offs among sustainable development goals (SDGs). *J. Clean. Prod.* **2019**, *232*, 474–486.
6. Wang, J.L.; Zhou, W.Q.; Pickett, S.T.A.; Yu, W.J.; Li, W.F. A multiscale analysis of urbanization effects on ecosystem services supply in an urban megaregion. *Sci. Total Environ.* **2019**, *662*, 824–833. [CrossRef] [PubMed]
7. Yao, Y.L.; Liu, P.X.; Chen, L.L.; Lu, L.P. Urban Extended Remote Sensing Analysis in Hefei City in the Last 30 Years. *Econ. Geogr.* **2013**, *9*, 65–72.
8. Reid, R.S.; Kruska, R.L.; Muthui, N.; Taye, A.; Wotton, S.; Wilson, C.J.; Mulatu, W. Land-use and land-cover dynamics in response to changes in climatic, biological and socio-political forces: The case of southwestern Ethiopia. *Landsc. Ecol.* **2000**, *15*, 339–355. [CrossRef]
9. Wang, G.X.; Shen, X.L. On the relationship between urbanization and heat island effect in Shanghai. *J. Subtrop. Resour. Environ.* **2010**, *5*, 1–11.
10. Jusuf, S.K.; Wong, N.H.; Hagen, E.; Anggoro, R.; Hong, Y. The influence of land use on the urban heat island in Singapore. *Habitat Int.* **2007**, *31*, 232–242. [CrossRef]
11. Rizwan, A.; Memon, Y.C.; Leung, L. A review on the generation, determination and mitigation of Urban Heat Island. *J. Environ. Sci.* **2008**, *1*, 120–128. [CrossRef]
12. Peng, S.L.; Zhou, K.; Ye, Y.H.; Li, J. Advances in the study of urban heat island effects. *Ecol. Environ.* **2005**, *4*, 574–579.
13. Hao, L.P.; Fang, Z.F.; Li, Z.L.; Liu, Z.Q.; He, J.H. The inter-annual climate change and heat island effect of Chengdu during the recent fifty years. *Sci. Meteorol. Sin.* **2007**, *27*, 648–654.
14. Wang, J.; Da, L.; Song, K.; Li, B.L. Temporal variations of surface water quality in urban, suburban and rural areas during rapid urbanization in Shanghai, China. *Environ. Pollut.* **2008**, *152*, 387–393. [CrossRef]
15. Yao, Y.L.; Liu, P.X.; Chen, L.L. The characteristics and causes of space-time change of heat island effect in Hefei based on remote sensing image. *J. Ecol.* **2013**, *12*, 3351–3359.
16. Si Salah, H.; Ait-Aoudia, S.; Rezgui, A.; Goldin, S.E. Change detection in urban areas from remote sensing data: A multidimensional classification scheme. *Int. J. Remote Sens.* **2019**, *17*, 6635–6679. [CrossRef]
17. Wong, K.; Zhang, Y.; Tsou, J.Y.; Li, Y. Assessing impervious surface changes in sustainable coastal land use: A case study in Hong Kong. *Sustainability* **2017**, *9*, 1029. [CrossRef]
18. Yao, X.; Chen, Y.; Zhang, Q.; Mou, Z.; Yao, X.; Ou, C. Assessment of the urban expansion and its impact on the eco-environment—A case study of Hefei municipal area. *Sustainability* **2022**, *14*, 10613. [CrossRef]

19. An, Y.; Tsou, J.Y.; Wong, K.; Zhang, Y.; Liu, D.; Li, Y. Detecting land use changes in a rapidly developing city during 1990–2017 using satellite imagery: A case study in Hangzhou Urban area, China. *Sustainability* **2018**, *10*, 3303. [CrossRef]

20. Zhang, J.; Wang, H.; Ma, L.; Wang, J.; Wang, J.; Wang, Z. Structural path decomposition analysis of resource utilization in China, 1997–2017. *J. Clean. Prod.* **2021**, *322*, 129006. [CrossRef]

21. Hefei Municipal People's Government. Available online: http://www.hefei.gov.cn/ (accessed on 15 May 2019).

22. Gu, D.Z.; Huang, H.F.; Gao, T.Y. Study on the evolution of urban spatial form in Hefei based on ecological perspective. *J. Chang. Univ.* **2019**, *4*, 109–114.

23. Geospatial Data Cloud. Available online: http://www.gscloud.cn (accessed on 15 May 2019).

24. Wang, H.T.; Zhang, Y.Z.; Tsou, J.Y.; Li, Y. Surface Urban Heat Island Analysis of Shanghai (China) Based on the Change of Land Use and Land Cover. *Sustainability* **2017**, *9*, 1538. [CrossRef]

25. Yan, Y.; Dong, X.L.; Li, Y. A comparative study on the classification method of remote sensing image supervision based on ENVI. *Beijing Mapp.* **2011**, *3*, 14–16.

26. Zhao, C.X.; Qian, L.X. Comparison of remote sensing image supervision classification and non-supervisory classification. *J. Henan Univ.* **2004**, *3*, 90–93.

27. Jing, W.J.; Liu, Z.K. Composite classification method of multi-category remote sensing images. *Environ. Remote Sens.* **1995**, *4*, 298–302.

28. Li, M.Z.; Zhang, P.Y. The classification of wetland vegetation in remote sensing images based on SAM algorithm. *For. Eng.* **2015**, *2*, 8–13.

29. Zhu, Y.H.; Yang, K. Remote sensing monitoring and space features of urban expansion in Kunming. *Digit. Technol. Appl.* **2013**, *1*, 98–99.

30. Tan, W.B.; Liu, B.; Zhang, Z.X.; Zhao, X.L.; Yi, L.; Wang, X. Extended remote sensing monitoring and analysis of the built-up area of Kunming in the past 30 years. *J. Earth Inform.* **2009**, *1*, 117–124.

31. Xu, H.Q. Remote sensing information extraction of urban building land based on compressed data dimension. *China J. Graph.* **2005**, *2*, 223–229.

32. Zhao, C.E.; Ding, W.R. Dynamic monitoring of vegetation cover in Longchuan River basin based on ENVI and GIS technology. *For. Surv. Plan.* **2013**, *5*, 14–18+44.

33. Yue, W.; Liu, H.M.; Sun, G.J. Monitoring of dynamic changes in vegetation cover in the Zuli River basin based on remote sensing and GIS technology. *J. Lanzhou Univ.* **2009**, *1*, 6–11+18.

34. Hu, Y.; Liu, L.Y.; Jia, J.H. Remote sensing monitoring of vegetation dynamics and ecological restoration in the mountainous areas of Beijing. *J. Appl. Ecol.* **2010**, *11*, 2876–2882.

35. Li, M.M.; Wu, B.F.; Yan, C.Z.; Zhou, W.F. Remote sensing estimation of vegetation cover in the upper reaches of Miyun Reservoir. *Resour. Sci.* **2004**, *4*, 153–159.

36. You, X.; Yan, L.M. Surface temperature inversion based on the algorithm of ETM+ image radiation conduction equation. *Sci. Technol. Inf. Dev. Econ.* **2009**, *27*, 134–136+138.

37. Atmospheric Correction Parameter Calculator. Available online: https://atmcorr.gsfc.nasa.gov (accessed on 15 May 2019).

38. Chen, Y. A preliminary exploration of the urban heat island effect based on Landsat8--taking Xiamen as an example. *Mapp. Spat. Geogr. Inf.* **2014**, *2*, 123–128.

39. Sun, K.; Lu, T.D. Comparison of supervised classification methods in the classification processing of remote sensing images. *Jiangxi Sci.* **2017**, *3*, 367–371+468.

40. Sun, B.Y.; Huang, C.L. Discussion on landscape planning and design in the ecological leisure area in the northern part of the Shushan Area of Hefei. *Agric. Sci. Technol. Inf.* **2014**, *6*, 67–72.

41. Bureau of Statistics, Anhui Province. Available online: http://tjj.hefei.gov.cn (accessed on 15 May 2019).

42. Jia, P.; Yang, G.Q. Analysis of the driving force of urban land expansion: Taking Hubei Province as an example. *Study Soil Water Conserv.* **2006**, *2*, 182–185.

43. Xu, Y.W. The Human history orientation of Hefei City Construction. *Contemp. Constr.* **2003**, *6*, 5–6.

44. Wu, X.; Fang, X.; Miao, Y.; Wang, K.; Pang, C. Study on urban expansion of Hefei city based on Landsat data. *J. Zhejiang Univ.* **2017**, *44*, 631–639.

45. World Weather. Available online: https://en.tutiempo.net (accessed on 15 May 2019).

46. Zhang, Y.; Jiang, P.; Chen, Y.Y.; Xiong, H.Y.; Zhang, Z.N. Study on the effect of Wuhan heat island based on Landsat TM image. *J. Ecol. Environ.* **2012**, *5*, 884–889.

47. Liu, B.; Bao, G.T.; Peng, K.; Shi, M.; He, H.L. Comparison of different surface temperature inversion algorithms based on Landsat TM images. *World Geogr. Inf.* **2015**, *3*, 57–61.